








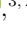








Virial Black Hole Masses for AGNs behind the Magellanic Clouds

SWAYAMTRUPTA PANDA ^{1,*}, SZYMON KOZŁOWSKI ², MARIUSZ GROMADZKI ², MARCIN WRONA ²,
PATRYK IWANEK ², ANDRZEJ UDALSKI ², MICHAŁ K. SZYMAŃSKI ², IGOR SOSZYŃSKI ², PAWEŁ PIETRUKOWICZ ²,
KRZYSZTOF ULACZYK ^{3,2}, JAN SKOWRON ², RADOSŁAW POLESKI ², PRZEMEK MRÓZ ², DOROTA M. SKOWRON ²,
KRZYSZTOF RYBICKI ^{4,2} AND MATEUSZ MRÓZ ²

¹*Laboratório Nacional de Astrofísica - MCTI, R. dos Estados Unidos, 154 - Nações, Itajubá - MG, 37504-364, Brazil*

²*Astronomical Observatory, University of Warsaw, Al. Ujazdowskie 4, 00-478 Warsaw, Poland*

³*Department of Physics, University of Warwick, Coventry CV4 7 AL, UK*

⁴*Department of Particle Physics and Astrophysics, Weizmann Institute of Science, Rehovot 76100, Israel*

(Accepted March 15, 2024)

Submitted to ApJS

ABSTRACT

We use the spectroscopic data collected by the Magellanic Quasars Survey (MQS) as well as the photometric V - and I -band data from the Optical Gravitational Lensing Experiment (OGLE) to measure the physical parameters for active galactic nuclei (AGNs) located behind the Magellanic Clouds. The flux-uncalibrated MQS spectra were obtained with the 4-m Anglo-Australian Telescope and the AAOmega spectroscope ($R = 1300$) in a typical ~ 1.5 hour visit. They span a spectral range of 3700–8500 Å and have S/N ratios in a range of 3–300. We report the discovery and observational properties of 161 AGNs in this footprint, which expands the total number of spectroscopically confirmed AGNs by MQS to 919. After the conversion of the OGLE mean magnitudes to the monochromatic luminosities at 5100 Å, 3000 Å, and 1350 Å, we were able to reliably measure the black hole masses for 165 out of 919 AGNs. The remaining physical parameters we provide are the bolometric luminosities as well as the Eddington ratios. A fraction of these AGNs have been observed by the OGLE survey since 1997 (all of them since 2001), enabling studies of correlations between the variability and physical parameters of these AGNs.

1. INTRODUCTION

The black hole mass, M_{BH} , in active galactic nuclei (AGNs), is the single most important physical parameter determining most of their properties. It influences the sizes of accretion disks, their innermost stable orbits, temperature profiles, or the spectral energy distribution shapes and luminosities. That is why the black hole mass is the primary parameter sought in AGNs.

Early reverberation mapping campaigns have enabled the first measurements of the black hole masses (e.g., Netzer & Peterson 1997; Gebhardt et al. 2000; Kaspi et al. 2000). These campaigns determined simultane-

ously the distance R to the broad-line-region (BLR) clouds, the time delay τ between the continuum variability and the responding emission lines ($R = c\tau$), and the velocity v of the BLR clouds. In principle, these two parameters are sufficient to determine the mass, as $M_{\text{BH}} \propto Rv^2$. Kaspi et al. (2000) realized that the BLR radius R is tightly correlated with the continuum luminosity L , as $R \propto L^{0.7}$, which is known as the radius–luminosity relation for AGNs. The relation was soon improved to yield $R \propto L^{0.5}$ (Bentz et al. 2006, 2009, 2013). Combining the radius–luminosity relation with the equation for the black hole mass, we end up with a simple prescription for the measurement of the black hole mass, as $M_{\text{BH}} \propto L^{0.5}v^2$. Since both the luminosity L and the velocity v can be simultaneously measured from a single AGN spectrum, it is straightforward nowadays to determine AGN black hole masses for massive spectroscopic surveys with hundreds of thousands

spanda@lna.br

simkoz@astrouw.edu.pl

* CNPq fellow

of AGN spectra (Shen et al. 2011; Rakshit et al. 2020; Wu & Shen 2022), albeit with the typical uncertainty of 0.4 dex.

In this paper, we measure the physical parameters (virial black hole masses, luminosities) for AGNs discovered behind the Magellanic Clouds by the Magellanic Quasars Survey (MQS; Kozłowski et al. 2011, 2012, 2013). These two nearby galaxies have been the primary target for microlensing and variability surveys since the early nineties, so a hundred million sources, that can be resolved from Earth, now have two to three decades-long photometric light curves. A combination of the photometric variability and physical parameters for AGNs is a way to improve our understanding of these objects (e.g., Kelly et al. 2009; Kozłowski 2016; Simm et al. 2016; Suberlak et al. 2021; Burke et al. 2021).

In Section 2, we present both photometric and spectroscopic data used in our analyses, while in Section 3, we elaborate on the methods used to calculate both monochromatic and bolometric luminosities, the methodology of fitting the AGN spectra, and the measurement of basic spectroscopic parameters, in particular FWHM of broad emission lines. This section concludes with the methodology and calculation of the black hole masses for our AGNs along with the corresponding Eddington ratios. The results are presented in Section 4 and discussed in Section 5. The paper is summarized in Section 6.

2. DATA

In this paper, we analyze spectra for AGNs discovered behind the Magellanic Clouds and obtained by the Magellanic Quasars Survey (Kozłowski et al. 2011, 2012, 2013). The ~ 4000 spectroscopically observed AGN candidates were selected based on their mid-IR and optical colors, optical variability in the OGLE-III survey, and the X-ray flux. They were observed with the 4-m Anglo-Australian Telescope (AAT) equipped with the AAOmega spectroscope, producing a resolution of $R \approx 1300$ inside a spectral range of 3700–8800 Å in the 580V (blue channel) and 385R (red channel) gratings. Most observations were 1.5h long (3×30 minutes) producing a signal-to-noise ratio of 3–300 with a median of about 40 for $I < 19.5$ mag sources (Kozłowski et al. 2011). The spectra were reduced with the AAOmega 2DFDR routines (Taylor et al. 1996). Kozłowski et al. (2013) reported the discovery of 758 AGNs.

We have re-inspected all the MQS spectra in this analysis and identified 161 additional AGNs, albeit faint (Table A1). This makes a sample of analyzed spectra contain a total of 919 AGNs.

We also use the V - and I -band light curves from the Optical Gravitational Lensing Experiment (OGLE; Udalski et al. 1997, 2008, 2015) to calculate both the monochromatic and bolometric AGN luminosities. The data have been collected since 1997 with the 1.3-m Warsaw Telescope located in Las Campanas Observatory, Chile.

A detailed methodology for analyzing both spectra and photometric data is presented in the next section.

3. METHODS

In this section, we provide details of the AGN monochromatic and bolometric luminosities calculation from the OGLE photometry, spectral fitting, and estimating of the black hole masses and Eddington luminosities.

3.1. Estimating the AGN monochromatic luminosities from photometry

The primary objective of the Magellanic Quasars Survey was to find and confirm as many AGNs behind the Magellanic Clouds as possible, to measure proper motions of the Clouds (e.g., Zivick et al. 2018) and to enable future AGN variability studies.

The spectroscopic AAT observations were taken in sub-optimal weather conditions and without the flux calibration procedure (unnecessary for finding redshifts). Therefore, we are unable to measure the monochromatic (and so bolometric) fluxes directly from these spectra.

Kozłowski (2015), however, provides a method to estimate the monochromatic fluxes from broad-band optical and IR photometry with a typical 0.1 dex uncertainty in a redshift range of $0.1 < z < 4.9$. Because most AGNs are variable sources, to estimate the weighted mean photometric magnitudes (obtained in the flux space), we use the long-term OGLE data in the V - and I -band filters, spanning up to 26 years. We then correct the mean observed magnitudes for the extinction using the reddening maps of the LMC and SMC from red clump stars (Skowron et al. 2021), adopting $A_I = 1.217 \times E(V - I)$ and $A_V = 2.217 \times E(V - I)$. Because the Skowron et al. (2021) maps provide the median reddening to the red clumps stars, which can be interpreted as the extinction to the center of their distribution in the LMC/SMC, we double the extinction correction to mimic the lines of sight extending all the way though these galaxies. We also calculate the k -corrections by using the composite SDSS AGN spectrum (Vanden Berk et al. 2001) and OGLE V and I filters (Udalski et al. 2015). Finally, we calculate the absolute V and I magnitudes for each AGN assuming a standard Λ CDM cosmological model with $(\Omega_\Lambda, \Omega_M, \Omega_k) = (0.72, 0.28, 0.0)$ and $H_0 = 70$

km s⁻¹ Mpc⁻¹ to calculate the distance modulus (DM). They are provided in Table A2.

We then follow the prescription of Kozłowski (2015) to calculate L_{5100} , L_{3000} , L_{1350} monochromatic fluxes (twice, one from the V - and one from I -band mean magnitude). For each monochromatic flux, we calculate the mean from V and I , and the final fluxes are provided in Table A2.

3.2. Spectral fitting with PYQSOFIT

We use PYQSOFIT for spectral decomposition (Guo et al. 2018) of all of our MQS AGN spectra. We correct the spectra to the rest frame and correct for Galactic extinction using the extinction curve of Cardelli et al. (1989) and the reddening map of Skowron et al. (2021). We then perform a host galaxy decomposition using galaxy eigenspectra from Yip et al. (2004a) as well as quasar eigenspectra from Yip et al. (2004b) implemented in PYQSOFIT code. If more than half of the pixels from the resulting host galaxy fit are negative, then the host galaxy and quasar eigenspectra fit are not applied.

We then fit the power law, UV/optical FeII, and Balmer continuum models utilizing the continuum fitting windows as described in Guo et al. (2018); Rakshit et al. (2020). The optical FeII emission template spans 3686-7484Å, from Boroson & Green (1992), while the UV FeII template spans 1000-3500Å, adopted from Vestergaard & Wilkes (2001); Tsuzuki et al. (2006); Salvander et al. (2007). PYQSOFIT fits these empirical FeII templates using a normalization, broadening, and wavelength shift. Next, we perform emission line fits, using Gaussian profiles as described in Shen et al. (2019) and Rakshit et al. (2020). Depending on redshift and spectral coverage, we fit the following emission lines: H α λ 6564.6 broad and narrow, [NII] λ λ 6549,6585, [SII] λ λ 6718,6732, H β λ 4861 broad and narrow, [OIII] λ λ 5007,4959, Mg II λ 2800 broad and narrow, and C IV λ 1549 broad and narrow. In addition, we also fitted the C III] λ 1909 and Ly α 1216¹ broad and narrow components but restricted our analysis and results in this work to the sources with fits in the broad H α , H β , Mg II, and C IV broad emission lines. We run all of these fits using Monte Carlo simulation based on the actual observed spectral error array, which in turn yields an error array for all our decomposition fits. An example spectral decomposition is shown in Figure 1². The host galaxy fits used in PYQSOFIT are limited to

rest-frame wavelengths between 3450 – 8000 Å. Due to this limitation, to fit the MgII line complex, we follow the prescription of Green et al. (2022) but make a conditional execution of host decomposition in the same run, i.e., if $z < 0.25$, then the host contribution is included. Otherwise, the host contribution is not accounted for. In our fitting routine using PYQSOFIT we fit the spectrum over the whole wavelength range, although for this work, we only use the measurements of the FWHMs of the broad emission lines (H β , MgII, and CIV). These profiles are fitted within narrow wavelength windows (\sim 100-150Å, e.g., as shown in the bottom panels in Figure 1) after the power-law continuum and host contribution are removed leaving only the emission line profiles to be fitted, and the effect from the absolute spectrophotometric calibration is minimal. This primarily affects the estimation of the continuum luminosities and therefore, we make use of the OGLE photometry-derived monochromatic luminosities throughout this work. We report the FWHMs for the H β , MgII, and CIV emission lines for our sources in Table A3.

3.3. Estimating black hole mass and Eddington ratios

To calculate the bolometric luminosity (L_{bol}), we follow the prescription of Richards et al. (2006); Shen et al. (2011); Rakshit et al. (2020), where the AGN monochromatic luminosity is scaled by a bolometric correction factor to estimate the L_{bol} :

$$L_{bol} = \begin{cases} 9.26 \times L_{5100} & \text{if } z < 0.8 \\ 5.15 \times L_{3000} & \text{if } 0.8 \leq z < 1.9 \\ 3.81 \times L_{1350} & \text{if } z \geq 1.9 \end{cases}$$

Next, the black hole mass (M_{BH}) can be estimated using the virial relation from the single-epoch spectrum for which continuum monochromatic luminosity (here derived from photometry) and line width measurements are available using the following relation:

$$\log \left(\frac{M_{BH}}{M_{\odot}} \right) = A + B \log \left(\frac{L_{\lambda}}{10^{44} \text{ erg s}^{-1}} \right) + 2 \log \left(\frac{\text{FWHM}}{\text{km s}^{-1}} \right), \quad (1)$$

where A and B are the constants empirically calibrated from prior studies. Following the prescription of Rakshit et al. (2020), we used the black hole mass calibrations from Vestergaard & Peterson (2006, hereafter VP06), and Vestergaard & Osmer (2009, hereafter VO09):

$$A, B = \begin{cases} (0.910, 0.50) & \text{for H}\beta, \text{VP06} \\ (0.860, 0.50) & \text{for MgII, VO09} \\ (0.660, 0.53) & \text{for CIV, VP06} \end{cases}$$

¹ We are successful in extracting useful fitted parameters for 13 and 2 sources for C III] and Ly α measurements, respectively.

² All fitted spectra from our sample can be found on this <https://ogle.astrouw.edu.pl/ogle4/MQS/>.

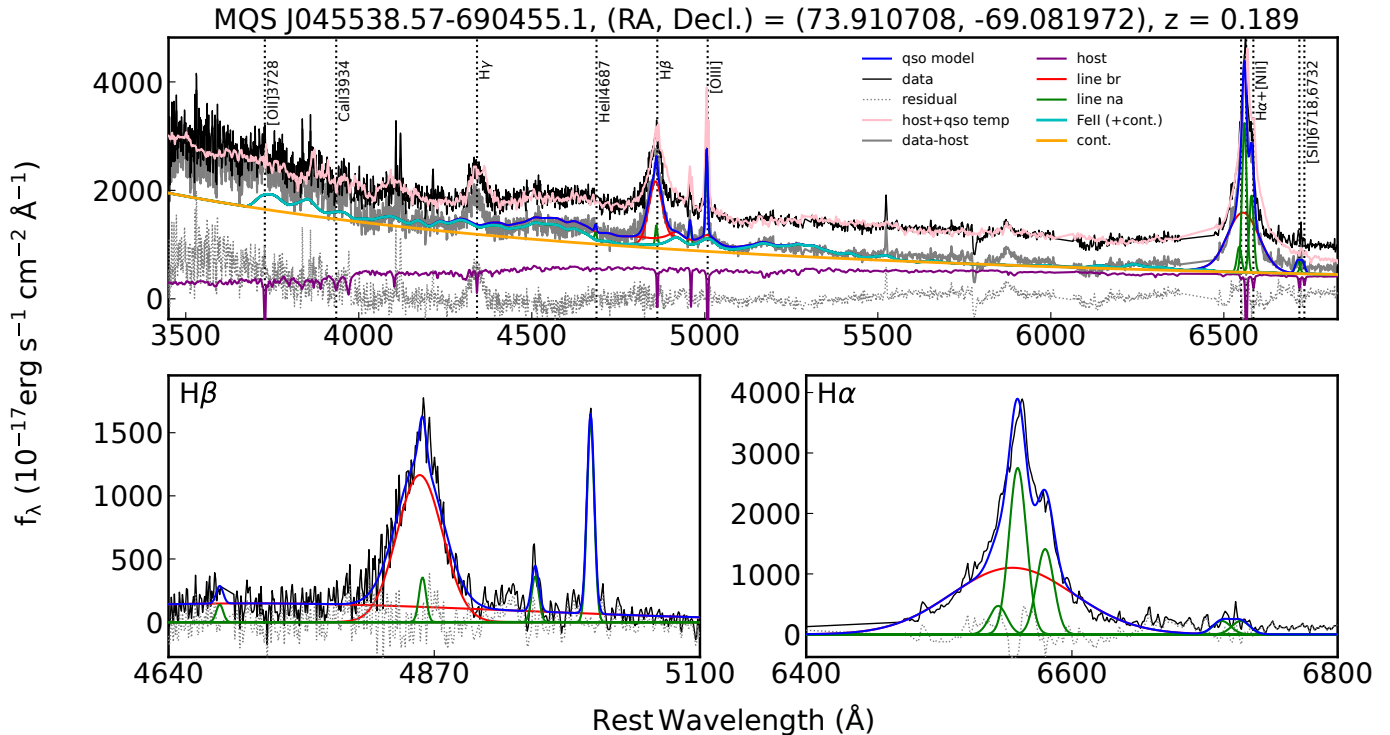


Figure 1. Exemplary fit using PyQSOFIT (Guo et al. 2018) for a quasar spectrum (MQS J045538.57-690455.1) without significant host-galaxy contribution. In each panel, we show the MQS data (black), power-law continuum (yellow), FeII pseudo-continuum (in addition to the power-law continuum, light green), broad emission lines (red), narrow emission lines (dark green), the total best-fit qso model (blue), which is the sum of continuum and emission lines. The host galaxy contribution is shown in magenta, while the host subtracted data is shown in a continuous gray line, and the sum of the host and qso model is shown in pink. *Upper panel:* The rest-frame central wavelengths for prominent emission lines are shown using the dashed vertical lines. The sky coordinates (in degrees), and the redshift for the sources are quoted in the title of the figure. *Lower panel:* a zoomed version of individual line complexes. The residuals are shown in dotted gray in each panel.

Subsequently, we estimate the Eddington ratio (λ_{Edd}), i.e. the ratio of the L_{bol} to the Eddington luminosity³ (L_{Edd}). The derived L_{bol} , M_{BH} , and λ_{Edd} for the sources in our sample are reported in Table A4. We do not account for the error on the constant term (A) while estimating the uncertainties on the BH masses (Sec. 3.4).

3.4. Error budget

In this subsection, we discuss the error budget for the black hole mass and luminosity measurements.

The black hole mass equation (Equation 1) contains four variables (A , B , L_{λ} , and FWHM). While the uncertainties for A and B typically are not reported, the usual dispersion of this relation is 0.3–0.4 dex (e.g., VP06). This means that a single measurement of the black hole mass has an uncertainty of about 0.4 dex.

The black hole mass, via Equation (1), also depends on FWHM, which is estimated along with its uncertainty by PyQSOFIT from fitting the broad emission lines,

³ $L_{\text{Edd}} \approx 1.26 \times 10^{38} \left(\frac{M_{\text{BH}}}{M_{\odot}} \right) \text{ erg s}^{-1}$.

and the monochromatic luminosity. The uncertainty of the latter is estimated as a combination of two factors: (1) the uncertainty of the conversion of the broad-band magnitudes to the monochromatic luminosities which is typical of the order of 0.1 dex, and (2) the uncertainty of the mean broad-band magnitude. The latter one depends not only on the photometric quality of the survey but also on the data length and number of points as AGNs are variable sources. The longer the light curve and the larger the number of photometric points, the closer the mean estimation is to the true mean. The contribution of this uncertainty to the total uncertainty is 0.004 dex.

4. RESULTS

4.1. Luminosity distribution as a function of redshift

In Figure 2, we demonstrate the dependence of the monochromatic luminosity on the redshift for the sources in our sample. The luminosities are derived from the photometry as described in Sec. 3.1. We highlight three cases of monochromatic luminosities: (a) at 5100Å, (b) at 3000 Å, and (c) at 1350 Å, which are in the

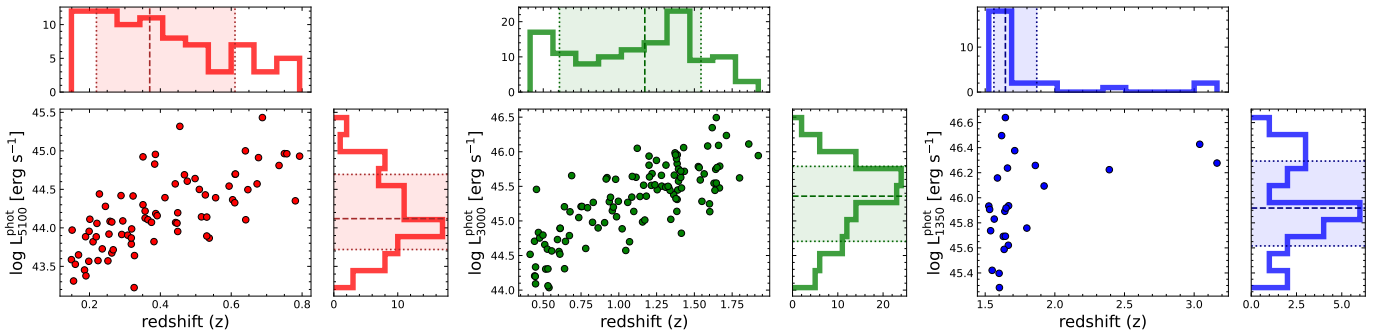


Figure 2. AGN luminosity at 5100Å (*left panel*), 3000Å (*middle panel*), and 1350Å (*right panel*) derived from the OGLE photometry as a function of redshift. The respective marginal distributions are shown per panel. The medians are marked with dashed lines and the shaded regions mark the region between 16th and 84th percentiles of the distributions in each of the marginal distributions.

Table 1. Properties of the monochromatic luminosity and redshift distributions

	N	Median	16 th percentile	84 th percentile
log L_{5100}	78	44.120	43.720	44.694
z	78	0.370	0.220	0.611
log L_{3000}	117	45.358	44.705	45.789
z	117	1.172	0.607	1.544
log L_{1350}	25	45.918	45.616	46.293
z	25	1.645	1.563	1.870

NOTE—The median, 16th and 84th percentile values are represented in respective panels in Figure 2 and are truncated to 3 decimal digits.

vicinity of the prominent broad emission lines, i.e., H β , MgII, and CIV, respectively. The properties (median and the 16th and 84th percentiles) for the respective joint distributions presented in Figure 2 are reported in Table 1.

To facilitate the comparison of the sources and their luminosities across redshift, we estimate the bolometric luminosities (using the prescription outlined in Sec. 3.3). Figure 3 demonstrates the bolometric luminosity (L_{bol}) as a function of redshift for all of the sources in our sample. The sources are colored based on the monochromatic luminosity used to estimate the respective L_{bol} values. We see a clear increase in the net L_{bol} with increasing redshift extending up to $z \sim 3.5$, where the bottom envelope is due to the limiting magnitude of the SDSS or MQS/OGLE surveys.

We overlay a filtered version of the SDSS DR14 QSO sample (Rakshit et al. 2020) on this distribution to compare the two distributions. The filtering of the sources is made by using the quality flags associated with the M_{BH} and L_{bol} estimations from Rakshit et al. (2020). They use QUAL flag = 0 to identify sources with reliable M_{BH} and L_{bol} estimations. We have chosen to use the two flags simultaneously to avoid confusion later when discussing the M_{BH} measurements from SDSS and our

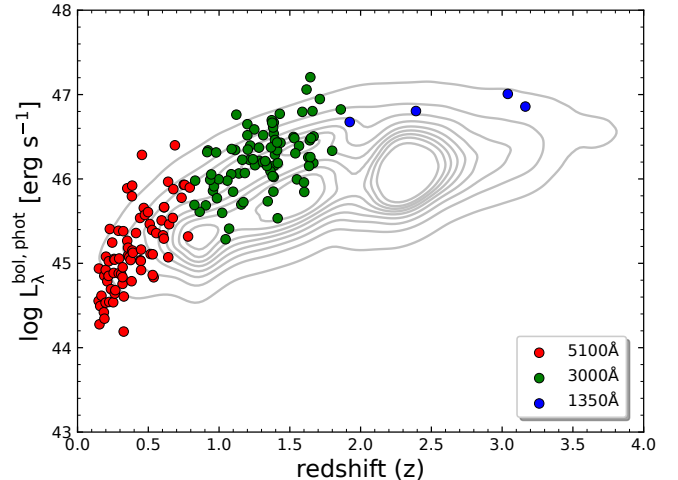


Figure 3. Bolometric luminosity as a function of redshift for the sources in our sample. The sources are colored by the AGN monochromatic luminosity used to estimate the bolometric luminosity. The sources from the SDSS DR14 QSO sample are shown using contours where the fiducial L_{bol} are reported with the QUAL flag = 0. We show 9 levels for the contour map, which correspond to the isodensity of the SDSS sources, with the outermost contour encompassing 90% of the sources and decreasing inwards by 10%.

sample. The original SDSS DR14 QSO sample contains 526,265 sources of which, after filtering, we are left with 449,863. We note here that before filtering the sample of sources in the SDSS many erroneous estimates were reported for the L_{bol} and M_{BH} with significantly large uncertainties. The filtering allowed us to remove sources with such measurements and limit ourselves to estimates with higher reliability. To highlight the large differences due to the filtering, we report the median, minimum, and maximum values for the redshift, L_{bol} and M_{BH} distributions for the original and the filtered SDSS samples in Table 2. In Figure 3, we show the filtered SDSS sample using contours. We use 9 levels for the contour map which correspond to the iso-density lines encompassing

Table 2. Properties from the SDSS DR14 QSO sample (original versus filtered sample)

original (526,265)	median	min	max
z	1.837	0.004	6.968
$\log L_{\text{bol}}$	45.938	29.745	48.304
$\log M_{\text{BH}}$	8.684	1.089	11.459
filtered (449,863)	median	min	max
z	1.784	0.038	5.033
$\log L_{\text{bol}}$	45.954	42.979	48.304
$\log M_{\text{BH}}$	8.675	5.991	11.050

NOTE—The median, minimum, and maximum values are truncated to 3 decimal digits. The filtered sample is prepared using the QUAL flag = 0 for the L_{bol} and M_{BH} simultaneously. The numbers in the parentheses denote the sources in each sample.

90% of the SDSS AGNs (the outermost contour) and decreasing inwards by 10%. We note that some of the sources in our sample (28) lie outside the lowest contour line, which is the consequence of differences in the surveys’ setups. We see an overall agreement between the two distributions with a clear increase in the L_{bol} with increasing redshift. Additionally, we note that sources in our sample have relatively higher L_{bol} values as compared to the peak of the SDSS distribution irrespective of the monochromatic luminosity used to estimate the L_{bol} values. This can be attributed to the shallower depth of the OGLE survey as compared to the SDSS survey.

4.2. Black hole mass and Eddington ratio distributions

In Figure 4, we demonstrate the $M_{\text{BH}}-M_{\text{BH}}$ planes estimated using the pairs of emission lines, i.e., ($\text{H}\alpha$, $\text{H}\beta$), ($\text{H}\beta$, MgII) and (MgII , CIV), respectively. We have 10 sources with simultaneously reliable $\text{H}\alpha$ -based and $\text{H}\beta$ -based M_{BH} measurements in our sample. Similarly, we have eight sources with reliable $\text{H}\beta$ -based and MgII -based M_{BH} measurements, and three sources with reliable MgII -based and CIV -based M_{BH} measurements. Overall, we find a good agreement between the masses estimated using FWHM from different emission lines and monochromatic luminosities, which are depicted using the line of unity (dashed line) in each panel of Figure 4. The scatter in the panels of Figure 4 can be attributed to either the relative offsets in the FWHM values between the lines, the monochromatic luminosities differences, and the uncertainty in the relations (i.e., mostly due to the constant term (B) associated with the monochromatic luminosity) used to derive the M_{BH} . We note, however, that we do not account for the error on

Table 3. Properties from the $\lambda_{\text{Edd}}-M_{\text{BH}}$ distribution for our sample

$\text{H}\beta$, 5100Å (70)	median	min	max
$\log \lambda_{\text{Edd}}$	-1.220	-2.859	-0.177
$\log M_{\text{BH}}$	8.234	7.271	9.515
MgII , 3000Å (97)	median	min	max
$\log \lambda_{\text{Edd}}$	-0.795	-1.615	-0.106
$\log M_{\text{BH}}$	8.838	8.051	9.495
CIV , 1350Å (7)	median	min	max
$\log \lambda_{\text{Edd}}$	-0.124	-0.721	0.130
$\log M_{\text{BH}}$	8.778	8.523	9.295

NOTE—The median, minimum, and maximum values are truncated to 3 decimal digits. The numbers in the parentheses denote the sources in each sub-sample.

the constant term (A, see Equation 1) while estimating the uncertainties on the BH masses.

Similarly to Figure 3, in Figure 4 we overlay the contours from the filtered SDSS sample. The SDSS catalog provides the M_{BH} mass measurements obtained using the $\text{H}\beta$, MgII , and CIV emission lines and respective monochromatic continuum luminosities (no $\text{H}\alpha$). Hence, we only show these contour maps for the middle ($\text{H}\beta$ -based M_{BH} versus MgII -based M_{BH}) and right (MgII -based M_{BH} versus CIV -based M_{BH}) panels. Contrary to the contour maps in Figure 3, we truncate the contours at 67% and above for the probability mass for the respective distributions for better visualization of the comparison between the two samples. We notice that all the measurements from our sample, including the uncertainties, lie within the threshold of the filtered SDSS sample.

In Figure 5, we present the Eddington ratio (λ_{Edd})– M_{BH} plane occupied by the sources in our sample. The sources are colored based on the respective emission lines and monochromatic continuum luminosities incorporated to estimate the λ_{Edd} and M_{BH} . We notice that the distribution shifts towards higher black hole masses and higher Eddington ratios as we move from ($\text{H}\beta$, 5100Å) based sub-sample to (MgII , 3000Å) and (CIV , 1350Å) sub-samples. This trend is also quantified in Table 3, where we see that the ranges covered by the $\text{H}\beta$ -based M_{BH} and λ_{Edd} are the widest. While the MgII -based sample is more concentrated at a slightly larger M_{BH} range but covers a subset of the range in the Eddington ratio relative to the $\text{H}\beta$ -based sub-sample. Finally, the CIV -based sample only contains seven sources, much smaller than the other two sub-samples (we have 70 and 97 sources, for the $\text{H}\beta$ -

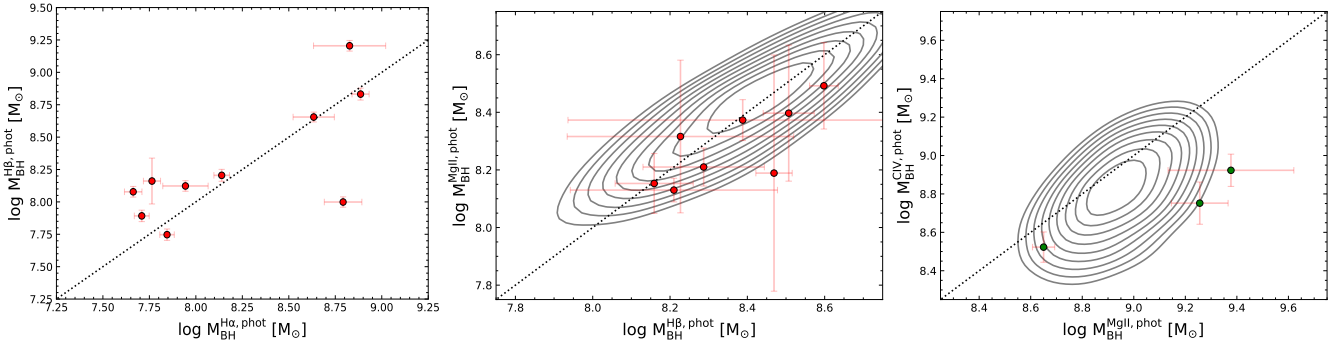


Figure 4. Comparison of the black hole mass estimates, *left panel*: for sources where both $H\alpha$ and $H\beta$ FWHMs are simultaneously available; *middle panel*: for sources where both $H\beta$ and $MgII$ FWHMs are simultaneously available; and *right panel*: for sources where both $MgII$ and CIV are simultaneously available in a spectrum. In each panel, the dotted black line represents the 1-to-1 line shown for reference. The sources from the SDSS DR14 QSO sample are shown using contours where the $H\beta$ -, $MgII$ - and CIV -based BH masses are reported (no $H\alpha$). For the SDSS sample, we filter the sources based on the fiducial L_{bol} and M_{BH} with the QUAL flags = 0. The largest contour represents 67% of the total number of the SDSS AGNs.

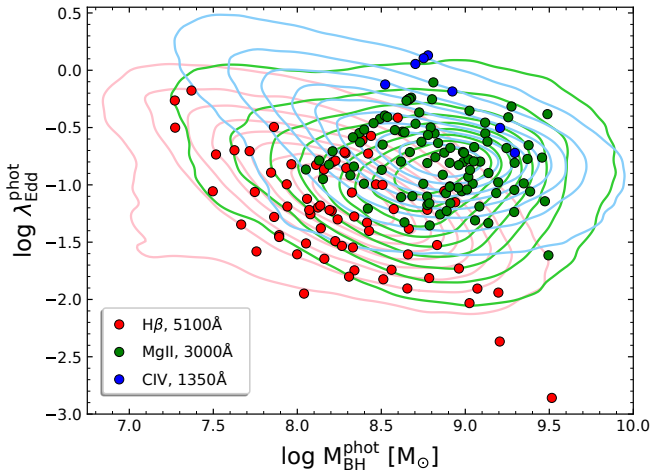


Figure 5. Black hole masses versus Eddington ratios for the sources in our sample. The sources are colored based on the monochromatic luminosity-emission line pairs. The sources from the SDSS DR14 QSO sample are shown using contours where the $H\beta$ - (in pink), $MgII$ - (in light green), and CIV -based (in light blue) BH masses are considered. The SDSS sources are filtered based on the adopted fiducial L_{bol} and M_{BH} with the QUAL flags = 0. We do not show the uncertainties associated with the M_{BH} and λ_{Edd} for the MQS AGNs for clarity.

based and $MgII$ -based sub-samples, respectively.), and occupies a region with the highest λ_{Edd} even going above the Eddington limit. Although, the M_{BH} range is relatively modest as compared to the other two sub-samples. Similar to the previous analyses, we overlay the corresponding contour maps from the filtered SDSS sample for the respective sub-samples. In this figure, the contour maps show the full range of the distribution from the filtered SDSS sample without any threshold cuts. We notice that the sources from both our and the SDSS sample occupy roughly the same region in the λ_{Edd} - M_{BH}

plane, albeit a few sources from the $H\beta$ sub-sample from our sample which has slightly lower Eddington ratio values as compared to their SDSS counterparts. We note here in passing, that the masses derived using the CIV region and $MgII$ region are comparable for our MQS quasars sample. This similarity between the M_{BH} estimates is also noted in the M_{BH} distributions derived from the SDSS DR14 sample (see Figure 6). We consider the sources where the quality flags for the M_{BH} is 0, i.e., the masses measurements are reliable. We independently show the masses estimated from the $H\beta$, $MgII$, and CIV regions which use the formalisms from Vestergaard & Peterson (2006), Vestergaard & Osmer (2009), and Vestergaard & Peterson (2006), respectively. The median values for each sub-sample are shown using dashed lines and the region between the 16th and 84th percentiles are shown using shaded colors per sub-sample. For $MgII$ - (green) and CIV -based (blue) sub-samples, we find that the distributions behave similarly, i.e., the respective medians are comparable (8.74 vs 8.71) and the regions bounded by the 16th and 84th percentiles also overlap. The overall similarity in M_{BH} using different broad emission lines has been noted in other studies (Assef et al. 2011; Kozłowski 2017a). We, however, note that the mass measurements can be affected by the choice of methodology (see e.g., Mejía-Restrepo et al. 2018; Dalla Bontà et al. 2020).

4.3. Optical plane of the Eigenvector 1

Understanding the diversity in spectral properties within AGNs poses a significant challenge. To this end, the work by Boroson & Green (1992) holds paramount importance for two key reasons. Firstly, it represents one of the pioneering contributions in AGN research employing Principal Component Analysis (PCA) to unravel the interrelation between observed quasar prop-

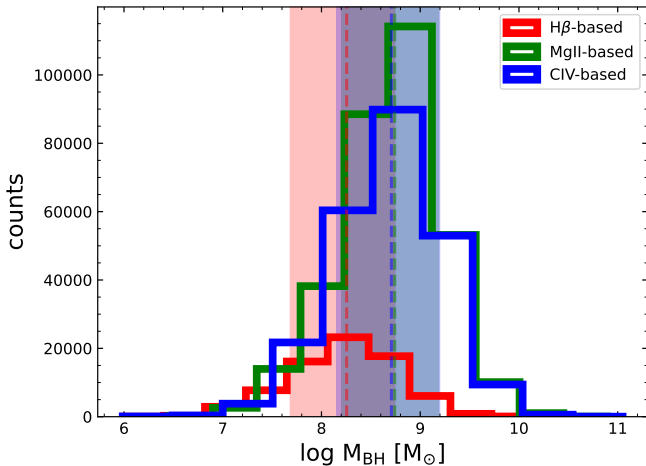


Figure 6. M_{BH} distributions from the *cleaned* SDSS DR14 QSO sample Rakshit et al. (2020). The H β - (red), MgII- (green), and CIV-based (blue) masses are shown in this histogram. The respective median values are shown using dashed lines of identical colors, while the shaded regions mark regions bounded by the 16th and 84th percentiles for the respective distributions.

erties. This analysis delves into the Main Sequence of Quasars, employing Eigenvectors, notably Eigenvector 1. This particular eigenvector reveals an intriguing anti-correlation between the equivalent width (EW) of the optical FeII blend (spanning 4434-4684 Å) and the peak intensity of the forbidden line [OIII] λ 5007 Å. Secondly, this study also establishes a connection between the FWHM of the broad H β emission and this eigenvector. This linkage, specifically between the FWHM of the broad H β line and the strength of the FeII blend (expressed as EW(FeII) relative to the EW of the broad component of H β , or R_{FeII}), has evolved into the well-established “Quasar Main Sequence”. This sequence, illustrated in the left panel of Figure 7, is primarily influenced by the Eddington ratio among other physical properties, as documented in subsequent studies (e.g., Sulentic et al. 2000; Shen & Ho 2014; Marziani et al. 2018; Panda et al. 2018, 2019a,b).

Furthermore, an additional classification system based on the width of the H β emission line profile in AGN spectra has been introduced, distinguishing between Population A and Population B. Population A encompasses local Narrow-Line Seyfert 1 galaxies (NLS1s) and more massive high accretors, primarily identified as radio-quiet sources (e.g., Marziani & Sulentic 2014), with $\text{FWHM}(\text{H}\beta) \lesssim 4000 \text{ km s}^{-1}$. Notably, Population A sources often exhibit a H β profile with a Lorentzian-like shape (e.g., Sulentic et al. 2002; Zamfir et al. 2010). In contrast, Population B sources, characterized by broader H β profiles ($\gtrsim 4000 \text{ km s}^{-1}$), are predominantly associ-

Table 4. Properties of the sample presented in the Quasar Main Sequence diagram in Figure 7

MQS (41)	median	min	max
z	0.351	0.151	0.647
$\log L_{5100}$	44.090	43.453	45.318
$\text{FWHM}(\text{H}\beta)$	3784.782	1436.520	11526.192
$\log M_{\text{BH}}$	8.331	7.273	9.205
$\log \lambda_{\text{Edd}}$	-1.276	-2.367	-0.414
R_{FeII}	0.526	< 0.001	2.378
SDSS (18762)	median	min	max
z	0.581	0.056	0.890
$\log L_{5100}$	44.539	42.769	46.267
$\text{FWHM}(\text{H}\beta)$	3709.279	925.010	18263.505
$\log M_{\text{BH}}$	8.341	6.560	9.936
$\log \lambda_{\text{Edd}}$	-0.952	-2.757	0.451
R_{FeII}	0.713	0.037	6.142

NOTE—The median, minimum, and maximum values are truncated to 3 decimal digits. The numbers in the parenthesis denote the sources in each sample.

ated with “jetted” characteristics (e.g., Padovani et al. 2017). These sources tend to exhibit Gaussian-shaped H β profiles, and for those with even higher FWHMs, disk-like double Gaussian profiles are observed in Balmer lines. The choice of the FWHM cutoff at 4000 km s^{-1} was proposed by Sulentic et al. (2000); Marziani et al. (2018), who observed more pronounced changes in AGN properties beyond this line-width threshold. Subsequent studies have shown that the two populations form a continuous link and share a connection (Fraix-Burnet et al. 2017; Berton et al. 2020). The morphology of the emission line profiles and the characteristics of the continuum are intricately linked to the central engine, specifically the black hole mass, accretion rate, black hole spin, and the viewing angle from a distant observer (Czerny et al. 2017; Marziani et al. 2018; Panda et al. 2018, 2019b; Panda 2021a).

In our sample, to check the location of the sources on the Eigenvector 1 sequence, we first filtered the sources where the relative uncertainties on the R_{FeII} and the $\text{FWHM}(\text{H}\beta)$ were below a certain threshold. We assume this limit to be 20% to keep reasonable measurements and avoid sources where these values could be unreliable or affected by low signal-to-noise spectral quality. This limits the total number of sources to 41/58, where 58 was the source count where we have a non-zero measurement for the R_{FeII} and $\text{FWHM}(\text{H}\beta)$. We tabulate the salient properties of this limited sample of 41 sources in Table 4. In the right panel of Figure 7, we demonstrate the optical plane of the Eigenvector 1 sequence for our sources.

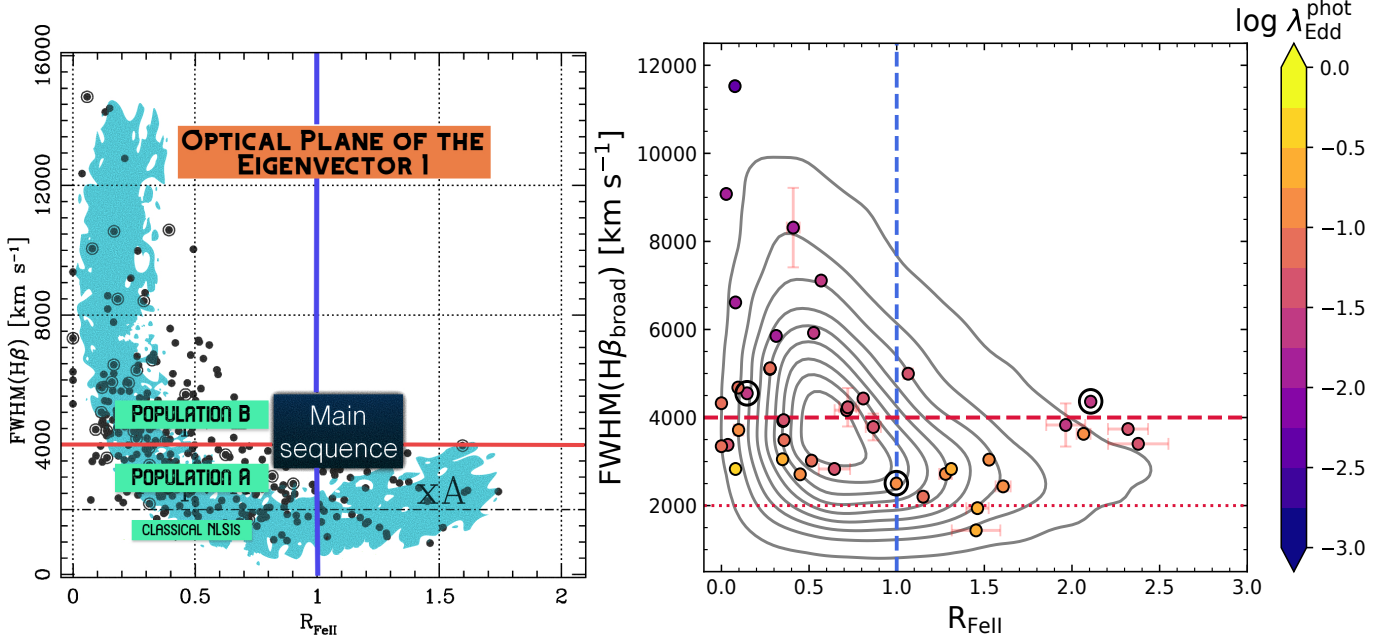


Figure 7. *Left panel:* Schematic diagram of the optical plane of the Eigenvector 1. Abridged version from Panda et al. (2020). The horizontal line denotes the threshold in $\text{FWHM}(\text{H}\beta)$ at 4000 km s^{-1} which separates the Population A and Population B sources. The “classical” NLS1s are located below the $\text{FWHM}(\text{H}\beta) \leq 2000 \text{ km s}^{-1}$ (dot-dashed line). The vertical blue line marks the limit for $R_{\text{FeII}} = 1$ separating the weak and strong FeII emitters (or xA sources). *Right panel:* The optical plane for the MQS sources. Similar to the left panel, the horizontal dashed and dotted lines represent the 4000 km s^{-1} and 2000 km s^{-1} thresholds, respectively, while the dashed vertical line marks the $R_{\text{FeII}} = 1$ limit. The sources are colored based on their Eddington ratios (in the log scale). Here, we demonstrate the sources where both the $\text{FWHM}(\text{H}\beta)$ and R_{FeII} are of high quality, i.e., corresponding errors are within 20% of the estimated values. The sources from the SDSS DR14 QSO sample are shown using contours where a similar quality filtering is adopted. Spectra for the three sources marked with the bulls-eyes are shown in Figure 8.

These sources are color-coded by their respective λ_{Edd} values. To facilitate the comparison between our sample and the filtered SDSS sample, we overlay the SDSS sample using contour maps. We find remarkable agreement between the two samples. Some of the sources from our sample do have slightly larger $\text{FWHM}(\text{H}\beta)$ and/or larger R_{FeII} estimates. We note, however, that the exact extent of the filtered and limited SDSS sample considered here does have a wider coverage (please see the lower half of the Table 4), although these sources constitute a minor fraction of the total sample considered here.

We highlight the spectra of three of our sources in Figure 8. These three sources are marked with bullseye symbols in Figure 7 and were chosen to demonstrate the variety in R_{FeII} measurements we have in our sample. The spectra have been binned for better visualization. We can see that going from the source with one of the lowest R_{FeII} measurements (spectrum in red), towards the source with one of the highest values for R_{FeII} (spectrum in blue), we see a substantial change in the FeII bump feature and the weakening of the $\text{H}\beta$ emission. This further demonstrates the efficacy of the

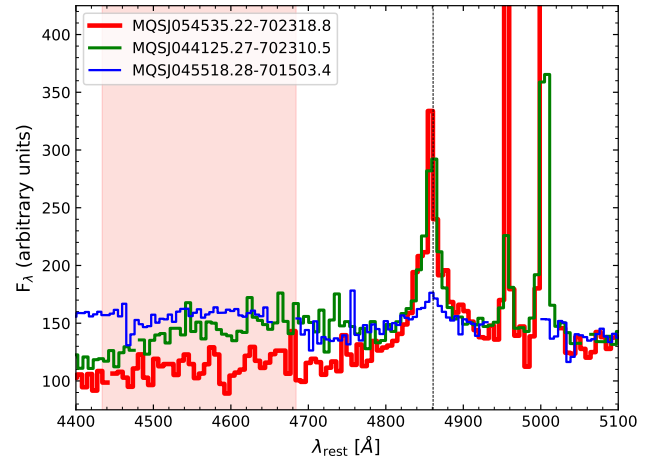


Figure 8. Binned spectra for the sources highlighted in the right panel of Figure 7, corresponding to three R_{FeII} regimes - low (in red, 0.146 ± 0.005), medium (in green, 0.998 ± 0.009), and high (in blue, 2.1068 ± 0.018). The shaded region shows the FeII range ($4434\text{--}4684\text{\AA}$) and the central wavelength for the $\text{H}\beta$ is marked using the dotted line.

quasar main sequence analysis and its potential to categorize a diverse population of Type-1 AGNs.

5. DISCUSSION

Measuring the physical parameters of AGNs appears to be a straightforward task nowadays, as a single spectrum for an AGN is typically necessary to measure the monochromatic and bolometric luminosities, the black hole mass, and the Eddington ratio. The prime example, where such measurements were reported for 526,265 AGNs is the SDSS DR14 QSO catalog by [Rakshit et al. \(2020\)](#) and the SDSS DR16 version with 750,414 AGNs ([Wu & Shen 2022](#)).

While the black hole mass sets the size of an accretion disk, the key to our understanding of the physical processes within the disk may be ciphered in the observed AGN variability patterns. Several theoretical variability timescales are predicted: the dynamical one, which is the time it takes the matter to orbit the black hole ($\tau_{\text{dyn}} = \sqrt{GM/r^3}$), the thermal timescale ($\tau_{\text{th}} = \alpha^{-1}\tau_{\text{dyn}}$), or the viscous timescale ($\tau_{\text{vis}} = \tau_{\text{th}}(r/h)^2$), where M is the black hole mass, r is the radial size of the disk, α is the viscosity, and h is the disk height (e.g., [Czerny 2004](#); [Kelly et al. 2009](#)).

In [Kelly et al. \(2009\)](#), authors analyze ~ 7.5 -year-long MACHO light curves for 15 AGNs and model them with the damped random walk (DRW) model. The resulting AGN variability timescales in that article are comparable to the rest-frame light curve lengths, which likely means they are unreliable ([Kozłowski 2017b](#); [Sánchez et al. 2017](#); [Suberlak et al. 2021](#); [Burke et al. 2021](#)). [Kozłowski \(2017b\)](#) showed that time scales derived for the ~ 9000 SDSS AGNs having eight-year-long light curves are also unreliable.

Because an AGN light curve length is the most important parameter that influences the reliability of the intrinsic time scale measurement ([Kozłowski 2017b, 2021](#)), a quest for the longest possible length has begun. For example [Suberlak et al. \(2021\)](#), used the Pan-STARRS1 data to extend the SDSS Stripe 82 quasar light curves to 15 years. A similar approach was used in [Burke et al. \(2021\)](#), where the authors used 20-year-long photometric light curves for SDSS Stripe 82 quasars.

The OGLE survey has surveyed the sky since 1992, and the Magellanic Clouds since 1997. There exist AGN light curves from OGLE spanning 26 years and are continuously growing. By providing the physical parameters for these sources, this article sets a pathway to the forthcoming studies on the relations between the physical AGN parameters and variability parameters.

6. SUMMARY

In this paper, we reanalyzed ~ 4000 spectra from the Magellanic Quasars Survey. In addition to the already reported 758 AGNs in [Kozłowski et al. \(2013\)](#), we dis-

covered 161 new AGNs, albeit very faint, so the total number of the MQS AGNs increases to 919.

The spectra for these 919 AGNs were fit with the PYQSOFIT code to measure the FWHM (and EW) for the broad lines common in AGNs: $\text{H}\alpha$, $\text{H}\beta$, MgII , and CIV , but also EW of FeII blend (reported as ratio to the EW $\text{H}\beta$; R_{FeII}).

Since the spectra were flux-uncalibrated (by design), we used empirical conversions of the broadband extinction-corrected V - and I -band mean OGLE magnitudes to the monochromatic luminosities from [Kozłowski \(2015\)](#). For all the sources, we also calculated the bolometric luminosities, k -corrections, distance moduli, and absolute magnitudes.

By combining the broad line FWHM with the monochromatic luminosities, we calculated the black hole masses for 165 AGNs, where the spectra had adequate quality to do so. Whenever two black hole mass measurements were simultaneously available from a single spectrum ($\text{H}\alpha$ - $\text{H}\beta$, $\text{H}\beta$ - MgII , or MgII - CIV), we checked if the two masses stayed in agreement, which was the case.

We also demonstrate the optical plane of the Eigenvector 1, or the quasar main sequence for the sub-sample (41/165) of our sources with reliable measurements of the FWHM($\text{H}\beta$) and the strength of the optical FeII emission, i.e., R_{FeII} . There is an overall agreement with the SDSS-based main sequence diagram where we notice a discernible trend – increasing Eddington ratio with an increase/decrease in the $R_{\text{FeII}}/\text{FWHM}(\text{H}\beta)$, along the main sequence as found in earlier works ([Sun & Shen 2015](#); [Marziani et al. 2018](#); [Panda et al. 2019b, 2020](#); [Zajaček et al. 2023](#)). The sources with $R_{\text{FeII}} \gtrsim 1$ will be especially interesting to follow-up in the optical and near-infrared spectral regions to characterize their variable nature and evaluate the strength of other low-ionization lines, e.g., CaII triplet (emitting at $\lambda 8498$, $\lambda 8542$, and $\lambda 8662$) and $\text{OI}\lambda 8446$ which are efficient proxy to reveal the physical conditions of the low-ionization line emitting region in such AGNs ([Martínez-Aldama et al. 2015](#); [Marinello et al. 2016, 2020](#); [Panda 2021b](#); [Martínez-Aldama et al. 2021a](#); [Panda 2021c](#); [Martínez-Aldama et al. 2021b](#)). Such targets have also been found to be of use to standardize the BLR radius-luminosity relation that can allow to employ quasars as standardizable distance indicators ([Martínez-Aldama et al. 2019](#); [Du & Wang 2019](#); [Panda & Marziani 2023](#); [Panda et al. 2023](#)).

The physical parameters of those AGNs, such as the black hole mass, the Eddington luminosity, or the bolometric luminosity will be invaluable for future AGN variability studies. The OGLE survey alone has collected for

some of these sources 26-years-long light curves (up to 19-years-long rest-frame) in I -band and slightly shorter V -band light curves which will be demonstrated in a forthcoming work.

- 1 SP acknowledges the financial support of the Conselho
- 2 Nacional de Desenvolvimento Científico e Tecnológico
- 3 (CNPq) Fellowships 300936/2023-0 and 301628/2024-6.
- 4 SK has been supported by the Polish National Science
- 5 Centre through grant number 2018/31/B/ST9/00334
- 6 and by the IDUB “Nowe Idee 2B” grant from the Uni-
- 7 versity of Warsaw, Poland.

Facilities: Anglo Australian Telescope, 1.3m Warsaw Telescope

Software: MATPLOTLIB (Hunter 2007); NUMPY (Oliphant 2015); SCIPY (Virtanen et al. 2020); ASTROPY (Astropy Collaboration et al. 2018); TOPCAT (Taylor 2005); PYQSOFIT (Guo et al. 2018)

REFERENCES

- Assef, R. J., Denney, K. D., Kochanek, C. S., et al. 2011, ApJ, 742, 93, doi: [10.1088/0004-637X/742/2/93](https://doi.org/10.1088/0004-637X/742/2/93)
- Astropy Collaboration, Price-Whelan, A. M., Sipőcz, B. M., et al. 2018, AJ, 156, 123, doi: [10.3847/1538-3881/aabc4f](https://doi.org/10.3847/1538-3881/aabc4f)
- Bentz, M. C., Peterson, B. M., Netzer, H., Pogge, R. W., & Vestergaard, M. 2009, ApJ, 697, 160, doi: [10.1088/0004-637X/697/1/160](https://doi.org/10.1088/0004-637X/697/1/160)
- Bentz, M. C., Peterson, B. M., Pogge, R. W., Vestergaard, M., & Onken, C. A. 2006, ApJ, 644, 133, doi: [10.1086/503537](https://doi.org/10.1086/503537)
- Bentz, M. C., Denney, K. D., Grier, C. J., et al. 2013, ApJ, 767, 149, doi: [10.1088/0004-637X/767/2/149](https://doi.org/10.1088/0004-637X/767/2/149)
- Berton, M., Björklund, I., Lähteenmäki, A., et al. 2020, Contributions of the Astronomical Observatory Skalnaté Pleso, 50, 270, doi: [10.31577/caosp.2020.50.1.270](https://doi.org/10.31577/caosp.2020.50.1.270)
- Boroson, T. A., & Green, R. F. 1992, ApJS, 80, 109, doi: [10.1086/191661](https://doi.org/10.1086/191661)
- Burke, C. J., Shen, Y., Blaes, O., et al. 2021, Science, 373, 789, doi: [10.1126/science.abg9933](https://doi.org/10.1126/science.abg9933)
- Cardelli, J. A., Clayton, G. C., & Mathis, J. S. 1989, ApJ, 345, 245, doi: [10.1086/167900](https://doi.org/10.1086/167900)
- Czerny, B. 2004, arXiv e-prints, astro, doi: [10.48550/arXiv.astro-ph/0409254](https://doi.org/10.48550/arXiv.astro-ph/0409254)
- Czerny, B., Li, Y.-R., Hryniewicz, K., et al. 2017, The Astrophysical Journal, 846, 154, doi: [10.3847/1538-4357/aa8810](https://doi.org/10.3847/1538-4357/aa8810)
- Dalla Bontà, E., Peterson, B. M., Bentz, M. C., et al. 2020, ApJ, 903, 112, doi: [10.3847/1538-4357/abbc1c](https://doi.org/10.3847/1538-4357/abbc1c)
- Du, P., & Wang, J.-M. 2019, ApJ, 886, 42, doi: [10.3847/1538-4357/ab4908](https://doi.org/10.3847/1538-4357/ab4908)
- Fraix-Burnet, D., Marziani, P., D’Onofrio, M., & Dultzin, D. 2017, Frontiers in Astronomy and Space Sciences, 4, 1, doi: [10.3389/fspas.2017.00001](https://doi.org/10.3389/fspas.2017.00001)
- Gebhardt, K., Kormendy, J., Ho, L. C., et al. 2000, ApJL, 543, L5, doi: [10.1086/318174](https://doi.org/10.1086/318174)
- Green, P. J., Pulgarin-Duque, L., Anderson, S. F., et al. 2022, arXiv e-prints, arXiv:2201.09123, <https://arxiv.org/abs/2201.09123>
- Guo, H., Shen, Y., & Wang, S. 2018, PyQSOFit: Python code to fit the spectrum of quasars, Astrophysics Source Code Library, record ascl:1809.008, <http://ascl.net/1809.008>
- Hunter, J. D. 2007, Computing in Science and Engineering, 9, 90, doi: [10.1109/MCSE.2007.55](https://doi.org/10.1109/MCSE.2007.55)
- Kaspi, S., Smith, P. S., Netzer, H., et al. 2000, ApJ, 533, 631, doi: [10.1086/308704](https://doi.org/10.1086/308704)
- Kelly, B. C., Bechtold, J., & Siemiginowska, A. 2009, ApJ, 698, 895, doi: [10.1088/0004-637X/698/1/895](https://doi.org/10.1088/0004-637X/698/1/895)
- Kozłowski, S. 2015, AcA, 65, 251, <https://arxiv.org/abs/1504.05960>
- . 2016, ApJ, 826, 118, doi: [10.3847/0004-637X/826/2/118](https://doi.org/10.3847/0004-637X/826/2/118)
- . 2017a, ApJS, 228, 9, doi: [10.3847/1538-4365/228/1/9](https://doi.org/10.3847/1538-4365/228/1/9)
- . 2017b, A&A, 597, A128, doi: [10.1051/0004-6361/201629890](https://doi.org/10.1051/0004-6361/201629890)
- . 2021, AcA, 71, 103, doi: [10.32023/0001-5237/71.2.2](https://doi.org/10.32023/0001-5237/71.2.2)
- Kozłowski, S., Kochanek, C. S., & Udalski, A. 2011, ApJS, 194, 22, doi: [10.1088/0067-0049/194/2/22](https://doi.org/10.1088/0067-0049/194/2/22)
- Kozłowski, S., Kochanek, C. S., Jacyszyn, A. M., et al. 2012, ApJ, 746, 27, doi: [10.1088/0004-637X/746/1/27](https://doi.org/10.1088/0004-637X/746/1/27)

- Kozłowski, S., Onken, C. A., Kochanek, C. S., et al. 2013, *ApJ*, 775, 92, doi: [10.1088/0004-637X/775/2/92](https://doi.org/10.1088/0004-637X/775/2/92)
- Marinello, M., Rodríguez-Ardila, A., Garcia-Rissmann, A., Sigut, T. A. A., & Pradhan, A. K. 2016, *ApJ*, 820, 116, doi: [10.3847/0004-637X/820/2/116](https://doi.org/10.3847/0004-637X/820/2/116)
- Marinello, M., Rodríguez-Ardila, A., Marziani, P., Sigut, A., & Pradhan, A. 2020, *MNRAS*, 494, 4187, doi: [10.1093/mnras/staa934](https://doi.org/10.1093/mnras/staa934)
- Martínez-Aldama, M. L., Czerny, B., Kawka, D., et al. 2019, *ApJ*, 883, 170, doi: [10.3847/1538-4357/ab3728](https://doi.org/10.3847/1538-4357/ab3728)
- Martínez-Aldama, M. L., Dultzin, D., Marziani, P., et al. 2015, *ApJS*, 217, 3, doi: [10.1088/0067-0049/217/1/3](https://doi.org/10.1088/0067-0049/217/1/3)
- Martínez-Aldama, M. L., Panda, S., & Czerny, B. 2021a, in XIX Serbian Astronomical Conference, Vol. 100, 287–293
- Martínez-Aldama, M. L., Panda, S., Czerny, B., et al. 2021b, *ApJ*, 918, 29, doi: [10.3847/1538-4357/ac03b6](https://doi.org/10.3847/1538-4357/ac03b6)
- Marziani, P., & Sulentic, J. W. 2014, *MNRAS*, 442, 1211, doi: [10.1093/mnras/stu951](https://doi.org/10.1093/mnras/stu951)
- Marziani, P., Dultzin, D., Sulentic, J. W., et al. 2018, *Frontiers in Astronomy and Space Sciences*, 5, 6, doi: [10.3389/fspas.2018.00006](https://doi.org/10.3389/fspas.2018.00006)
- Mejía-Restrepo, J. E., Lira, P., Netzer, H., Trakhtenbrot, B., & Capellupo, D. M. 2018, *Nature Astronomy*, 2, 63, doi: [10.1038/s41550-017-0305-z](https://doi.org/10.1038/s41550-017-0305-z)
- Netzer, H., & Peterson, B. M. 1997, in *Astrophysics and Space Science Library*, Vol. 218, *Astronomical Time Series*, ed. D. Maoz, A. Sternberg, & E. M. Leibowitz, 85, doi: [10.1007/978-94-015-8941-3_8](https://doi.org/10.1007/978-94-015-8941-3_8)
- Oliphant, T. 2015, *NumPy: A guide to NumPy*, 2nd edn., USA: CreateSpace Independent Publishing Platform. <http://www.numpy.org/>
- Padovani, P., Alexander, D. M., Assef, R. J., et al. 2017, *Astronomy & Astrophysics*, 25, 2, doi: [10.1007/s00159-017-0102-9](https://doi.org/10.1007/s00159-017-0102-9)
- Panda, S. 2021a, Ph.D. Thesis, Centrum Fizyki Teoretycznej, Polskiej Akademii Nauk. <https://www.cft.edu.pl/przewody-doktorskie/przewod-doktorski-mgra-swayamtrupta-panda>
- . 2021b, *A&A*, 650, A154, doi: [10.1051/0004-6361/202140393](https://doi.org/10.1051/0004-6361/202140393)
- Panda, S. 2021c, in XIX Serbian Astronomical Conference, Vol. 100, 333–338
- Panda, S., Czerny, B., Adhikari, T. P., et al. 2018, *The Astrophysical Journal*, 866, 115, doi: [10.3847/1538-4357/aae209](https://doi.org/10.3847/1538-4357/aae209)
- Panda, S., Czerny, B., Done, C., & Kubota, A. 2019a, *The Astrophysical Journal*, 875, 133, doi: [10.3847/1538-4357/ab11cb](https://doi.org/10.3847/1538-4357/ab11cb)
- Panda, S., & Marziani, P. 2023, *Frontiers in Astronomy and Space Sciences*, 10, 1130103, doi: [10.3389/fspas.2023.1130103](https://doi.org/10.3389/fspas.2023.1130103)
- Panda, S., Marziani, P., & Czerny, B. 2019b, *The Astrophysical Journal*, 882, 79, doi: [10.3847/1538-4357/ab3292](https://doi.org/10.3847/1538-4357/ab3292)
- . 2020, *Contributions of the Astronomical Observatory Skalnaté Pleso*, 50, 293, doi: [10.31577/caosp.2020.50.1.293](https://doi.org/10.31577/caosp.2020.50.1.293)
- Panda, S., Marziani, P., Czerny, B., Rodríguez-Ardila, A., & Pozo Nunez, F. 2023, arXiv e-prints, arXiv:2311.13298, doi: [10.48550/arXiv.2311.13298](https://doi.org/10.48550/arXiv.2311.13298)
- Rakshit, S., Stalin, C. S., & Kotilainen, J. 2020, *ApJS*, 249, 17, doi: [10.3847/1538-4365/ab99c5](https://doi.org/10.3847/1538-4365/ab99c5)
- Richards, G. T., Lacy, M., Storrie-Lombardi, L. J., et al. 2006, *ApJS*, 166, 470, doi: [10.1086/506525](https://doi.org/10.1086/506525)
- Salviander, S., Shields, G. A., Gebhardt, K., & Bonning, E. W. 2007, *ApJ*, 662, 131, doi: [10.1086/513086](https://doi.org/10.1086/513086)
- Sánchez, P., Lira, P., Cartier, R., et al. 2017, *ApJ*, 849, 110, doi: [10.3847/1538-4357/aa9188](https://doi.org/10.3847/1538-4357/aa9188)
- Shen, Y., & Ho, L. C. 2014, *Nature*, 513, 210, doi: [10.1038/nature13712](https://doi.org/10.1038/nature13712)
- Shen, Y., Richards, G. T., Strauss, M. A., et al. 2011, *ApJS*, 194, 45, doi: [10.1088/0067-0049/194/2/45](https://doi.org/10.1088/0067-0049/194/2/45)
- Shen, Y., Hall, P. B., Horne, K., et al. 2019, *ApJS*, 241, 34, doi: [10.3847/1538-4365/ab074f](https://doi.org/10.3847/1538-4365/ab074f)
- Simm, T., Salvato, M., Saglia, R., et al. 2016, *A&A*, 585, A129, doi: [10.1051/0004-6361/201527353](https://doi.org/10.1051/0004-6361/201527353)
- Skowron, D. M., Skowron, J., Udalski, A., et al. 2021, *ApJS*, 252, 23, doi: [10.3847/1538-4365/abcb81](https://doi.org/10.3847/1538-4365/abcb81)
- Suberlak, K. L., Ivezić, Ž., & MacLeod, C. 2021, *ApJ*, 907, 96, doi: [10.3847/1538-4357/abc698](https://doi.org/10.3847/1538-4357/abc698)
- Sulentic, J. W., Marziani, P., Zamanov, R., et al. 2002, *ApJL*, 566, L71, doi: [10.1086/339594](https://doi.org/10.1086/339594)
- Sulentic, J. W., Zwitter, T., Marziani, P., & Dultzin-Hacyan, D. 2000, *ApJL*, 536, L5, doi: [10.1086/312717](https://doi.org/10.1086/312717)
- Sun, J., & Shen, Y. 2015, *ApJL*, 804, L15, doi: [10.1088/2041-8205/804/1/L15](https://doi.org/10.1088/2041-8205/804/1/L15)
- Taylor, K., Bailey, J., Wilkins, T., Shortridge, K., & Glazebrook, K. 1996, in *Astronomical Society of the Pacific Conference Series*, Vol. 101, *Astronomical Data Analysis Software and Systems V*, ed. G. H. Jacoby & J. Barnes, 195
- Taylor, M. B. 2005, in *Astronomical Society of the Pacific Conference Series*, Vol. 347, *Astronomical Data Analysis Software and Systems XIV*, ed. P. Shopbell, M. Britton, & R. Ebert, 29
- Tsuzuki, Y., Kawara, K., Yoshii, Y., et al. 2006, *ApJ*, 650, 57, doi: [10.1086/506376](https://doi.org/10.1086/506376)

- Udalski, A., Kubiak, M., & Szymanski, M. 1997, *AcA*, 47, 319, doi: [10.48550/arXiv.astro-ph/9710091](https://doi.org/10.48550/arXiv.astro-ph/9710091)
- Udalski, A., Szymanski, M. K., Soszynski, I., & Poleski, R. 2008, *AcA*, 58, 69, doi: [10.48550/arXiv.0807.3884](https://doi.org/10.48550/arXiv.0807.3884)
- Udalski, A., Szymański, M. K., & Szymański, G. 2015, *AcA*, 65, 1, doi: [10.48550/arXiv.1504.05966](https://doi.org/10.48550/arXiv.1504.05966)
- Vanden Berk, D. E., Richards, G. T., Bauer, A., et al. 2001, *AJ*, 122, 549, doi: [10.1086/321167](https://doi.org/10.1086/321167)
- Vestergaard, M., & Osmer, P. S. 2009, *ApJ*, 699, 800, doi: [10.1088/0004-637X/699/1/800](https://doi.org/10.1088/0004-637X/699/1/800)
- Vestergaard, M., & Peterson, B. M. 2006, *ApJ*, 641, 689, doi: [10.1086/500572](https://doi.org/10.1086/500572)
- Vestergaard, M., & Wilkes, B. J. 2001, *ApJS*, 134, 1, doi: [10.1086/320357](https://doi.org/10.1086/320357)
- Virtanen, P., Gommers, R., Oliphant, T. E., et al. 2020, *Nature Methods*, 17, 261, doi: [10.1038/s41592-019-0686-2](https://doi.org/10.1038/s41592-019-0686-2)
- Wu, Q., & Shen, Y. 2022, *ApJS*, 263, 42, doi: [10.3847/1538-4365/ac9ead](https://doi.org/10.3847/1538-4365/ac9ead)
- Yip, C. W., Connolly, A. J., Szalay, A. S., et al. 2004a, *AJ*, 128, 585, doi: [10.1086/422429](https://doi.org/10.1086/422429)
- Yip, C. W., Connolly, A. J., Vanden Berk, D. E., et al. 2004b, *AJ*, 128, 2603, doi: [10.1086/425626](https://doi.org/10.1086/425626)
- Zajaček, M., Panda, S., Pandey, A., et al. 2023, arXiv e-prints, arXiv:2310.03544, doi: [10.48550/arXiv.2310.03544](https://doi.org/10.48550/arXiv.2310.03544)
- Zamfir, S., Sulentic, J. W., Marziani, P., & Dultzin, D. 2010, *Monthly Notices of the Royal Astronomical Society*, 403, 1759, doi: [10.1111/j.1365-2966.2009.16236.x](https://doi.org/10.1111/j.1365-2966.2009.16236.x)
- Zivick, P., Kallivayalil, N., van der Marel, R. P., et al. 2018, *ApJ*, 864, 55, doi: [10.3847/1538-4357/aad4b0](https://doi.org/10.3847/1538-4357/aad4b0)

APPENDIX

Table A1. Observational parameters for the new 161 MQS AGNs (full version available electronically).

Name	RA	Dec	z	DM	mean V	mean I	Ext V	Ext I	K corr V	K corr I	Mag V	Mag I	L _{5100Å}	L _{3000Å}	L _{1350Å}
	hh:mm:ss.ss	dd:mm:ss.ss		Mpc	(obs)	(obs)	(abs.)	(abs.)	(abs.)	(abs.)	(abs.)	(abs.)	(erg s ⁻¹)	(erg s ⁻¹)	(erg s ⁻¹)
MQS J043443.27-695400.0	04:34:43.27	-69:54:00.00	1.215	44.653	19.979	19.414	0.235	0.129	-0.395	0.087	-24.749	-25.584	--	45.346±0.051	--
MQS J043445.71-690859.9	04:34:45.71	-69:08:59.90	0.562	42.584	21.83	20.635	0.206	0.113	-0.199	0.185	-20.967	-22.36	43.772±0.073	43.95±0.07	--
MQS J043501.08-701323.8	04:35:01.08	-70:13:23.80	1.335	44.908	--	--	0.259	0.142	-0.385	0.017	--	--	--	--	--
MQS J043522.52-703223.1	04:35:22.52	-70:32:23.10	0.412	41.773	21.717	20.295	0.364	0.2	-0.055	0.235	-20.729	-22.113	43.704±0.075	43.831±0.091	--
MQS J043541.79-702931.7	04:35:41.79	-70:29:31.70	1.345	44.928	20.197	19.251	0.337	0.185	-0.385	0.013	-25.02	-26.06	--	45.493±0.044	--
MQS J043553.04-685953.7	04:35:53.04	-68:59:53.70	0.723	43.253	--	--	0.251	0.138	-0.29	0.167	--	--	--	--	--
MQS J043617.19-701031.8	04:36:17.19	-70:10:31.80	0.967	44.036	19.141	18.501	0.284	0.156	-0.423	0.223	-25.04	-26.07	--	45.5±0.048	--
MQS J043625.99-700735.9	04:36:25.99	-70:07:35.90	1.777	45.678	20.734	18.722	0.284	0.156	-0.512	-0.162	-25	-27.106	--	45.741±0.053	45.874±0.082
MQS J043635.15-693656.5	04:36:35.15	-69:36:56.50	1.297	44.83	--	--	0.251	0.138	-0.388	0.035	--	--	--	--	--
MQS J043657.20-703824.7	04:36:57.20	-70:38:24.70	0.657	42.998	21.416	20.845	0.397	0.218	-0.251	0.173	-22.125	-22.762	44.058±0.074	44.269±0.058	--
MQS J043742.14-693310.1	04:37:42.14	-69:33:10.10	0.97	44.044	19.803	19.502	0.244	0.134	-0.424	0.222	-24.305	-25.032	--	45.153±0.048	--
MQS J043825.54-703614.6	04:38:25.54	-70:36:14.60	1.49	45.204	20.234	19.151	0.41	0.225	-0.385	-0.039	-25.405	-26.464	--	45.644±0.049	--
MQS J043845.15-692821.1	04:38:45.15	-69:28:21.10	1.361	44.96	20.903	20.071	0.295	0.162	-0.386	0.008	-24.261	-25.221	--	45.174±0.05	--
MQS J043900.74-693906.6	04:39:00.74	-69:39:06.60	1.306	44.848	19.749	19.047	0.302	0.166	-0.388	0.03	-25.315	-26.163	--	45.576±0.051	--
MQS J043904.58-680349.6	04:39:04.58	-68:03:49.60	0.846	43.675	--	19.436	0.164	0.09	-0.376	0.24	--	-24.659	--	44.61±	--
MQS J043908.00-683015.0	04:39:08.00	-68:30:15.00	1.358	44.954	21.381	20.701	0.191	0.105	-0.385	0.009	-23.57	-24.472	--	44.886±0.05	--
MQS J043925.47-674256.1	04:39:25.47	-67:42:56.10	1.42	45.074	20.077	18.69	0.177	0.097	-0.382	-0.01	-24.969	-26.568	--	45.595±0.046	--
MQS J044002.72-681538.4	04:40:02.72	-68:15:38.40	0.557	42.56	21.679	20.452	0.155	0.085	-0.195	0.187	-20.996	-22.465	43.802±0.073	43.979±0.07	--
MQS J044003.65-673216.0	04:40:03.65	-67:32:16.00	0.759	43.384	--	--	0.151	0.083	-0.336	0.186	--	--	--	--	--
MQS J044055.81-681833.7	04:40:55.81	-68:18:33.70	0.409	41.754	21.374	20.142	0.155	0.085	-0.052	0.237	-20.638	-22.019	43.667±0.075	43.793±0.091	--
MQS J044142.86-673239.6	04:41:42.86	-67:32:39.60	0.972	44.05	--	20.706	0.137	0.075	-0.425	0.221	--	-23.715	--	44.235±	--
MQS J044153.90-684535.3	04:41:53.90	-68:45:35.30	1.78	45.683	20.503	19.788	0.255	0.14	-0.513	-0.162	-25.177	-26.013	--	45.513±0.053	45.65±0.082
MQS J044245.58-693000.6	04:42:45.58	-69:30:00.60	1.199	44.617	20.049	19.364	0.324	0.178	-0.395	0.097	-24.821	-25.706	--	45.383±0.05	--
MQS J044312.02-694537.4	04:43:12.02	-69:45:37.40	1.61	45.413	19.965	19.115	0.282	0.155	-0.449	-0.114	-25.563	-26.494	--	45.69±0.047	45.838±0.092
MQS J044416.36-684215.0	04:44:16.36	-68:42:15.00	2.54	46.631	20.318	19.522	0.321	0.176	-0.696	-0.162	-26.259	-27.299	--	--	46.088±0.06
MQS J044417.49-693700.4	04:44:17.49	-69:37:00.40	1.429	45.091	19.726	18.979	0.288	0.158	-0.382	-0.013	-25.559	-26.415	--	45.671±0.049	--
MQS J044515.85-672555.2	04:45:15.85	-67:25:55.20	0.555	42.551	20.261	20.692	0.211	0.116	-0.194	0.19	-22.518	-22.281	44.144±0.073	44.319±0.07	--
MQS J044548.15-694041.9	04:45:48.15	-69:40:41.90	0.35	41.355	20.337	18.984	0.361	0.198	-0.007	0.193	-21.733	-22.96	--	--	--
MQS J044600.79-681704.8	04:46:00.79	-68:17:04.80	0.549	42.522	21.238	20.782	0.288	0.158	-0.19	0.185	-21.67	-22.241	43.903±0.065	44.076±0.067	--
MQS J044644.59-673544.4	04:46:44.59	-67:35:44.40	1.354	44.946	20.849	19.902	0.235	0.129	-0.385	0.01	-24.182	-25.312	--	45.176±0.047	--
MQS J044726.40-673055.6	04:47:26.40	-67:30:55.60	1.667	45.507	20.34	19.297	0.259	0.142	-0.479	-0.144	-25.206	-26.35	--	45.592±0.049	45.736±0.087
MQS J044758.66-664953.0	04:47:58.66	-66:49:53.00	0.78	43.457	--	--	0.259	0.142	-0.355	0.198	--	--	--	--	--
MQS J044758.91-671242.1	04:47:58.91	-67:12:42.10	1.525	45.267	21.265	20.148	0.295	0.162	-0.39	-0.052	-24.202	-25.391	--	45.187±0.053	45.381±0.073
MQS J044827.18-694337.7	04:48:27.18	-69:43:37.70	0.256	40.569	21.702	19.329	0.308	0.169	-0.013	-0.015	-19.496	-21.563	43.455±0.086	--	--
MQS J044830.07-663837.4	04:48:30.07	-66:38:37.40	0.449	41.996	20.085	19.266	0.184	0.101	-0.092	0.238	-22.187	-23.17	44.196±0.07	44.334±0.082	--
MQS J044922.60-664435.3	04:49:22.60	-66:44:35.30	0.595	42.735	21.807	20.188	0.186	0.102	-0.217	0.178	-21.083	-22.929	43.921±0.067	44.11±0.069	--
MQS J045051.09-671505.8	04:50:51.09	-67:15:05.80	1.645	45.471	20.279	19.357	0.204	0.112	-0.469	-0.136	-25.131	-26.202	--	45.547±0.052	45.693±0.091
MQS J045058.16-671634.4	04:50:58.16	-67:16:34.40	0.979	44.069	--	--	0.204	0.112	-0.427	0.218	--	--	--	45.538±0.052	--
MQS J045107.05-673800.9	04:51:07.05	-67:38:00.90	1.665	45.503	21.039	20.097	0.191	0.105	-0.479	-0.143	-24.367	-25.473	--	45.249±0.049	45.393±0.087
MQS J045242.83-674236.2	04:52:42.83	-67:42:36.20	0.492	42.234	21.823	20.576	0.12	0.066	-0.136	0.211	-20.515	-22.001	43.626±0.073	43.78±0.074	--
MQS J045253.95-674504.9	04:52:53.95	-67:45:04.90	1.334	44.906	--	--	0.126	0.069	-0.386	0.017	--	--	--	--	--
MQS J045424.28-680952.7	04:54:24.28	-68:09:52.70	0.319	41.12	21.789	21.18	0.284	0.156	-0.003	0.049	-19.902	-20.301	43.254±0.077	--	--
MQS J045525.06-704421.6	04:55:25.06	-70:44:21.60	0.769	43.419	20.222	19.504	0.268	0.147	-0.347	0.192	-23.386	-24.401	44.593±0.075	44.843±0.055	--
MQS J045632.58-670100.8	04:56:32.58	-67:01:00.80	1.087	44.352	20.144	19.6	0.224	0.123	-0.426	0.175	-24.23	-25.173	--	45.159±0.046	--
MQS J045651.08-680918.0	04:56:51.08	-68:09:18.00	1.34	44.918	20.897	20.221	0.293	0.161	-0.385	0.015	-24.222	-25.034	--	45.131±0.044	--

NOTE.—Columns are as follows: (1) MQS name; (2) right ascension (RA) in hh:mm:ss.ss; (3) declination (Dec) in dd:mm:ss.ss; (4) redshift (z); (5) distance modulus (DM); (6) mean observed magnitude in V-band; (7) mean observed magnitude in I-band; (8) Extinction in V-band; (9) Extinction in I-band; (10) K-corrected magnitude in V-band; (11) K-corrected magnitude in I-band; (12) absolute magnitude in V-band; (13) absolute magnitude in I-band; (14) monochromatic AGN luminosity estimated at 5100Å using photometric scaling (in log-scale); (15) monochromatic AGN luminosity estimated at 3000Å using photometric scaling (in log-scale); and (16) monochromatic AGN luminosity estimated at 1350Å using photometric scaling (in log-scale).

Table A2. Observational parameters for the 165 MQS AGNs (full version available electronically).

Name	RA	Dec	z	DM	mean V	mean I	Ext V	Ext I	K corr V	K corr I	Mag V	Mag I
	hh:mm:ss.ss	dd:mm:ss.ss		Mpc	(obs)	(obs)					(abs.)	(abs.)
MQS J053159.69–691951.6	05:31:59.69	–69:19:51.60	0.149	39.255	18.96	18.18	0.228	0.125	–0.065	–0.062	–20.686	–21.263
MQS J052402.28–701108.7	05:24:02.28	–70:11:08.70	0.151	39.287	17.942	17.193	0.18	0.099	–0.062	–0.062	–21.643	–22.230
MQS J050502.09–694504.0	05:05:02.09	–69:45:04.00	0.155	39.349	20.151	18.659	0.268	0.147	–0.06	–0.061	–19.674	–20.923
MQS J050634.04–691048.3	05:06:34.04	–69:10:48.30	0.16	39.425	21.242	17.62	0.228	0.125	–0.059	–0.056	–18.580	–21.999
MQS J051716.95–704402.0	05:17:16.95	–70:44:02.00	0.169	39.556	19.626	17.77	0.191	0.105	–0.055	–0.055	–20.257	–21.941

NOTE—Columns are as follows: (1) MQS name; (2) right ascension (RA) in hh:mm:ss.ss; (3) declination (Dec) in dd:mm:ss.ss; (4) redshift (z); (5) distance modulus (DM); (6) mean observed magnitude in V-band; (7) mean observed magnitude in I-band; (8) Extinction in V-band; (9) Extinction in I-band; (10) K-correction in V-band; (11) K-correction in I-band; (12) absolute magnitude in V-band; and (13) absolute magnitude in I-band

Table A3. AGN monochromatic luminosities and FWHMs for prominent broad emission lines for the 165 MQS AGNs (full version available electronically).

Name	$L_{5100\text{\AA}}$	$L_{3000\text{\AA}}$	$L_{1350\text{\AA}}$	FWHM($H\alpha$)	FWHM($H\beta$)	FWHM(MgII)	FWHM(CIV)
	(erg s^{-1})	(erg s^{-1})	(erg s^{-1})	(km s^{-1})	(km s^{-1})	(km s^{-1})	(km s^{-1})
MQS J053159.69–691951.6	43.587 ± 0.073	–	–	2759 ± 10	3373 ± 30	–	–
MQS J052402.28–701108.7	43.971 ± 0.073	–	–	7617 ± 1382	11526 ± 64	–	–
MQS J050502.09–694504.0	43.310 ± 0.073	–	–	–	3386 ± 4915	–	–
MQS J050634.04–691048.3	43.527 ± 0.059	–	–	9347 ± 767	3919 ± 49	–	–
MQS J051716.95–704402.0	43.649 ± 0.076	–	–	2831 ± 27	4376 ± 703	–	–

NOTE—Columns are as follows: (1) MQS name; (2) monochromatic AGN luminosity estimated at 5100Å using photometric scaling (in log-scale); (3) monochromatic AGN luminosity estimated at 3000Å using photometric scaling (in log-scale); (4) monochromatic AGN luminosity estimated at 1350Å using photometric scaling (in log-scale); (5) Full-width at half maximum (FWHM) of the broad $H\alpha$ profile; (6) FWHM of the broad $H\beta$ profile; (7) FWHM of the broad MgII profile; and (8) FWHM of the broad CIV profile.

Table A4. AGN bolometric luminosities, black hole masses, and Eddington ratios for the 165 MQS AGNs. (full version available electronically).

Name	$L_{\text{bol}}^{5100\text{\AA}}$	$L_{\text{bol}}^{3000\text{\AA}}$	$L_{\text{bol}}^{1350\text{\AA}}$	$M_{\text{BH}}^{H\alpha}$	$M_{\text{BH}}^{H\beta}$	$M_{\text{BH}}^{\text{MgII}}$	$M_{\text{BH}}^{\text{CIV}}$	$\lambda_{\text{Edd}}^{H\beta}$	$\lambda_{\text{Edd}}^{\text{MgII}}$	$\lambda_{\text{Edd}}^{\text{CIV}}$
	(erg s^{-1})	(erg s^{-1})	(erg s^{-1})	(M_{\odot})	(M_{\odot})	(M_{\odot})	(M_{\odot})	(5100Å)	(3000Å)	(1350Å)
MQS J053159.69–691951.6	44.554 ± 0.073	–	–	7.709 ± 0.040	7.892 ± 0.044	–	–	-1.439 ± 0.117	–	–
MQS J052402.28–701108.7	44.938 ± 0.073	–	–	8.827 ± 0.194	9.205 ± 0.041	–	–	-2.367 ± 0.114	–	–
MQS J050502.09–694504.0	44.277 ± 0.073	–	–	–	7.757 ± 1.297	–	–	-1.581 ± 1.369	–	–
MQS J050634.04–691048.3	44.494 ± 0.059	–	–	8.792 ± 0.101	7.999 ± 0.040	–	–	-1.606 ± 0.099	–	–
MQS J051716.95–704402.0	44.616 ± 0.076	–	–	7.764 ± 0.046	8.161 ± 0.177	–	–	-1.645 ± 0.253	–	–

NOTE—Columns are as follows: (1) MQS name; (2) Bolometric luminosity (L_{bol}) estimated using the $L_{5100\text{\AA}}$ (in log-scale); (3) L_{bol} estimated using the $L_{3000\text{\AA}}$ (in log-scale); (4) L_{bol} estimated using the $L_{1350\text{\AA}}$ (in log-scale); (5) Black hole mass (M_{BH}) estimated using the $L_{5100\text{\AA}}$ and FWHM($H\alpha$) (in log-scale); (6) M_{BH} estimated using the $L_{5100\text{\AA}}$ and FWHM($H\beta$) (in log-scale); (7) M_{BH} estimated using the $L_{3000\text{\AA}}$ and FWHM(MgII) (in log-scale); (8) M_{BH} estimated using the $L_{1350\text{\AA}}$ and FWHM(CIV) (in log-scale); (9) Eddington ratio (λ_{Edd}) estimated using the L_{bol} from 5100Å and $H\beta$ -based M_{BH} (in log-scale); (10) λ_{Edd} estimated using the L_{bol} from 3000Å and MgII-based M_{BH} (in log-scale); and (11) λ_{Edd} estimated using the L_{bol} from 1350Å and CIV-based M_{BH} (in log-scale). We note however that we do not account for the error on the constant term (A, see Equation 1) while estimating the uncertainties on the BH masses.